

Research Article

The Bonding Mechanism and Experimental Verification of Pilger Hot Rolling Clad Tube

Zonglin He ^{1,2}, Zhibing Chu,¹ Yuanhua Shuang,¹ and Yujun Gou¹

¹Shanxi Provincial Key Laboratory of Metallurgical Equipment Design and Technology, Taiyuan University of Science and Technology, No. 66 Waliu Road, Wanbolin District, Taiyuan 030024, Shanxi, China

²Mechanical Engineering Department, Shanxi Engineering Vocational College, No. 131 Xinjian Road, Taiyuan 030009, Shanxi, China

Correspondence should be addressed to Zonglin He; b20160002@stu.tyust.edu.cn

Received 4 July 2020; Revised 3 September 2020; Accepted 7 September 2020; Published 21 September 2020

Academic Editor: Jean-Michel Bergheau

Copyright © 2020 Zonglin He et al. This is an open access article distributed under the Creative Commons Attribution License, which permits unrestricted use, distribution, and reproduction in any medium, provided the original work is properly cited.

In this paper, we focus on the bonding mechanism of bimetallic clad tube because of its low cost and comprehensive properties. The numerical simulation and the experiment are carried out from the diffusion behavior of carbon atoms in the metallurgical bonding process. Based on the dislocation density model of Kocks, the tube billets are rolled by pilger hot rolling; the outer tube is 06Cr₁₉Ni₁₀ stainless steel, the inner tube is Q235 carbon steel, and the wall thickness ratio is 1:1. The research shows that the diffusion ability of carbon atoms mainly depends on the degree of the plastic strain in the stainless steel hot rolling process; there is positive correlation between the thickness of bonding carburized layer and the dislocation density produced by plastic deformation of stainless steel. The thickness difference of circumferential carburized layer in the deformation zone is larger than that near the finishing zone. Furthermore, a lot of contaminants cannot be completely metallurgically bonded between 20% and 30% reduction ratios; the contaminants near the bonding layer are refined and completely bonded metallurgically between 30% and 60% reduction ratios; the contaminants are further refined above 60% to 70% reduction ratio.

1. Introduction

The bimetallic clad tube has the comprehensive properties of two types of materials, such as the corrosion resistance of stainless steel, high stiffness of carbon steel, and low cost. Furthermore, it maximizes the realization of complementary materials, saves alloying elements, and reduces the engineering cost. The corrosion resistance and wear resistance of the tube are improved while ensuring the performance of the primary tube, and the service life of the tube is extended. It is the substitute product of pure stainless steel tube, copper tube, or other corrosion-resistant alloy tubes [1–3].

The technology of the bimetallic clad tube mainly includes mechanical bonding and metallurgical bonding process. The metallurgical bonding process has a higher bonding strength than the mechanical bonding process. Nowadays, the metallurgical bonding process mainly includes the centrifugal casting bonding, explosion welding

bonding, hot extrusion bonding, and hot rolling bonding [4]. Gong poured the liquid metal with different components into layers [5], controlled the inner and outer metal fusion layer at a certain wall thickness, and formed a complete metallurgical bonding. The disadvantages are that the casting easily produces segregation, and the casting surface is rough. Fan and Xu created sufficient impact from the explosion to make two kinds of metal bonded metallurgically [6], but this process produces chemical pollution, noise pollution, and more danger. The similar seamless steel tube method of NKK Corporation of Japan and Spain Extrusion Forming Steel Tube Company can produce metallurgical clad tubes with diameters of 60.3~219.1 mm using thermal perforation [7], but it is limited to piercing and cannot achieve high precision production.

The hot rolling bonding process has high efficiency and low cost. There have been some studies on this topic at home and abroad [8, 9], but there are few reports about the hot

rolling seamless bimetallic clad steel tube technology. To better explore the formability of hot rolled bimetallic clad tubes, this paper first proposes the technology of pilger hot rolling bimetallic clad tubes and studies the mechanism of the metallurgical bonding, which lays a foundation for the development of pilger hot rolling bimetallic clad steel tubes.

2. Analysis of the Bonding Mechanism of Pilger Hot Rolling Carbon Steel/Stainless Steel Tube

2.1. Bonding Mechanism of Hot Rolling Carbon Steel/Stainless Steel. The difference between the mechanical bonding carbon steel/stainless steel and the hot rolling metallurgical bonding is whether the atomic diffusion takes place in the bonding layer. In Figure 1(a), carbon steel and stainless steel are in the initial state at high temperature. Figure 1(b) shows that the contaminants are broken in the bonding layer and the internal metal structures of both sides will meet when the contaminants are continuously broken and refined under the plastic deformation [10]. The grains of stainless steel are refined and dislocated a lot in the plasticized state. Carbon atoms in carbon steel acquire higher atomic activation energy at high temperature and begin to diffuse into a large number of new grain boundaries caused by dislocations in stainless steel [11–13]. The carburized layer, the decarburized layer, and the interface finally appear [14], as shown in Figures 1(c) and 1(d).

Because carbon atoms in carbon steel are much smaller in size than Fe atoms and other alloying elements such as Cr and Ni in stainless steel, they can be diffused in the iron lattice by the gap diffusion mechanism, while the atoms like Cr and Ni can be diffused by vacancy diffusion mechanism. Since less atomic activation energy is required in the gap diffusion than that in vacancy diffusion, carbon atoms are diffused more easily [15].

2.2. Dislocation Theory Model. This paper uses the dislocation density model of Kocks [16], represented by the following equation:

$$\rho = \frac{h}{r} - \frac{h - \rho_0 r}{r} \cdot \exp(-r\varepsilon), \quad (1)$$

where ρ is dislocation density; ρ_0 is initial dislocation density; ε is strain; h is work-hardening coefficient; r is dynamic recovery softening coefficient.

In the early stage of stainless steel hot deformation, that is, before the critical strain, work hardening leads to the increase of dislocation density, while dynamic recovery leads to the decrease of dislocation density. However, work hardening plays a major role and dynamic recovery has little effect. Therefore, the dislocation density of stainless steel increases with strain. Here, h and r are multiplication terms and can be regarded as constant with respect to strain. There is positive correlation between ρ and ε .

2.3. Pilger Hot Rolling Model. Pilger rolling is a basic process of the seamless steel tube. The tube billet is rolled by the pass with the variable section, which gradually shrinks to reduce

the diameter and wall. As shown in Figure 2, the electromagnetic induction heating device is fixed on the moving stand of the rolling mill and moves synchronously with the rollers at 1200°C. The upper and the lower rollers with the variable section reciprocate under the crank slider mechanism. The tube billet is sheathed outside the mandrel whose cross section is gradually reduced. At two limited positions of the rolling stand, the tube billet is fed in the roll direction according to a certain feed; meanwhile, the tube billet is rotated once along the mandrel center line at a fixed angle, so that one period of rolling is completed. Finally, the tube billet can be completely rolled by multiple periodic rolling. The reciprocating pass disperses the plastic change of the metal that is periodically fed into the entire effective rolling process, uses the plasticity of the metal, and increases the reduction rate to 70–90% with the smaller rolling force [17], so it is the most effective processing method to fully use the plasticity of the material.

2.4. Analysis on the Stress State of Pilger Hot Rolling Clad Tube. The rollers of a pilger mill pass with variable sections along the axial direction [18], as shown in Figure 3. In the cross section, the rolling groove is an arc, the radius is $R(x)$, the eccentricity is $B(x)$ with the rolling center of the tube, and the roll gap is $H(x)$ [19]. Since the rolling groove is not concentric with the steel tube, a clearance appears on the side of the steel tube from point I on top of the roller to point II on the side of the roller and subsequently to gap III. $B(x)$ gradually changes from maximum to zero from the inlet to the outlet of the steel tube, and the rolling groove coincides with the center of the mandrel in the finishing zone. Figure 4 shows the stress states of the clad tube in the deformation zone and finishing zone. Area I is in the one-dimensional tensile stress and two-dimensional compressive stress state, area II is in the three-dimensional compressive stress state, and area III is in the one-dimensional tensile stress state. The finishing zone is in the three-dimensional compressive stress state because $B(x) = 0$.

3. Finite Element Model

3.1. Numerical Simulation. Due to the limitation of the finite element calculation and the complexity of the pilger hot rolling clad tube process, the model must be simplified [20]. By using a 3D software to establish each component, import the DEFORM-3D Ver 6.1 and position, as shown in Figure 5. The model consists of an upper roller, a lower roller, a clad tube billet, a pusher, and a mandrel, where X direction is the feeding direction of steel tube.

The simulation parameters of the pilger hot rolling bimetallic clad tube are shown in Table 1.

4. Experimental Procedures

The rolling experiment of the clad tube was performed with pilger LG30 mill in a factory. The size of the clad tube billet is 38 mm in outer diameter and 7 mm in wall thickness, while the outer diameter of finished tube is 24 mm and the wall thickness is 2 mm. The outer and the inner tube billets of the

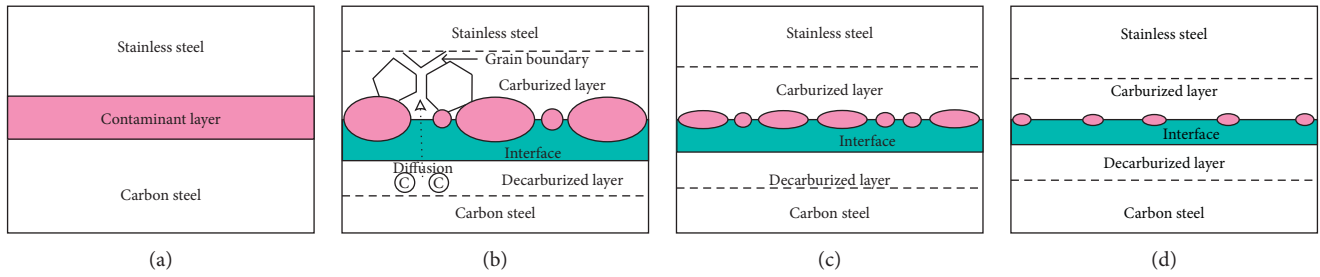


FIGURE 1: The bonding mechanism of hot rolling carbon steel/stainless steel. (a) Initial state. (b) Diffusion process of carbon atom. (c) Contaminants refinement process. (d) Further refinement of contaminants.

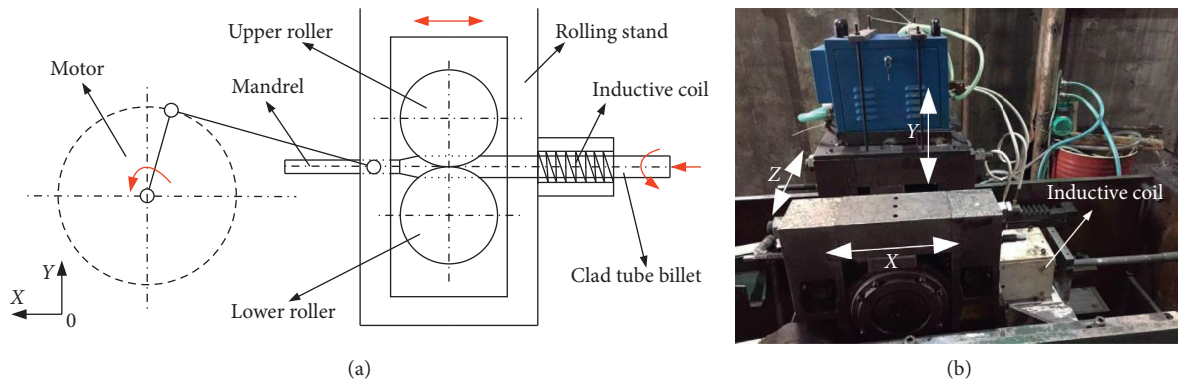


FIGURE 2: The pilger hot rolling clad tube principle diagram. (a) Schematic diagram. (b) Equipment.

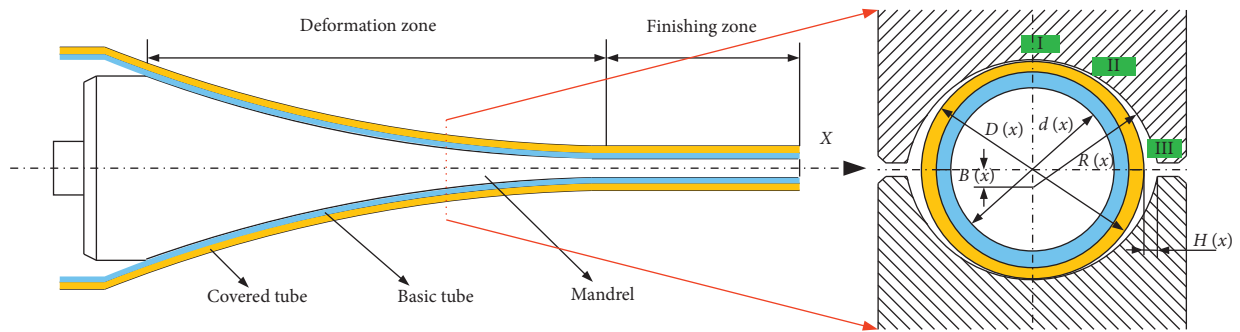


FIGURE 3: The pilger hot rolling clad tube pass expansion diagram.

clad tube were treated with oil film removal and oxide skin removal. Then, the outer and inner tubes were packaged together by welding at both ends. The vacuum degree between the billets was controlled to 0.1 Pa by welding at both ends and vacuumizing the billets, as shown in Figure 6(a). The experimental rolling process is shown in Figure 6(b). The process parameters are shown in Tables 2–4.

When the rolling process was finished, the samples were cut from the plastic deformation section and prepared for metallographic corrosion and electrolytic polishing technologies at six positions with different reduction rates from two groups of the rolled clad pieces, as shown in Figure 6(c). Herein, the inner metal and the outer metal were etched, respectively. The carbon steel was etched with 4% ethanol solution of nitric acid while the stainless steel was etched

with 10% chromic acid electrolytic method for microstructure observation. Then, the microstructure of stainless steel clad tube was observed by using SEM.

5. Results and Discussion

5.1. Diffusion Mechanism of Carbon Atoms. The pilger hot rolling bimetallic clad tube has large plastic deformation. It can be seen from Figure 4 that the tensile stresses in area I and area III along the X direction cause serious stretch and dislocation with longer grain near the surface of the metal contact and junction dramatic expansion of the metal surface. A more intense surface expansion corresponds to a greater bareness of the metal at the interface and more fresh metal extrusion from cracking. According to the film theory

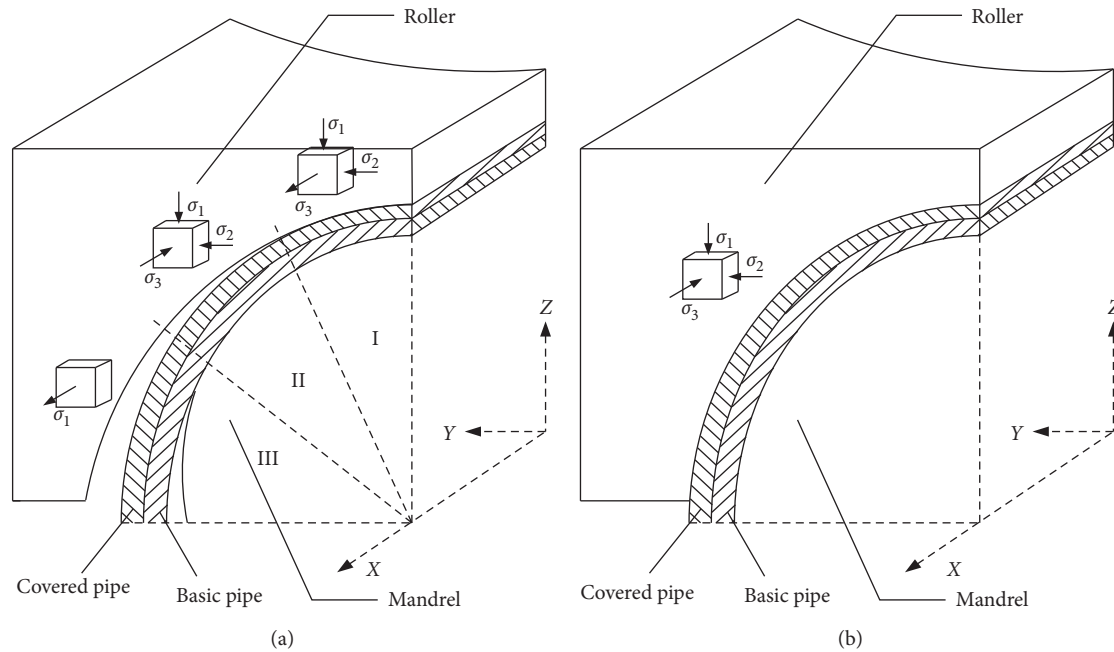


FIGURE 4: The stress state in deformation zone and finishing zone of pilger hot rolling bimetall clad tube. (a) Deformation zone. (b) Finishing zone.

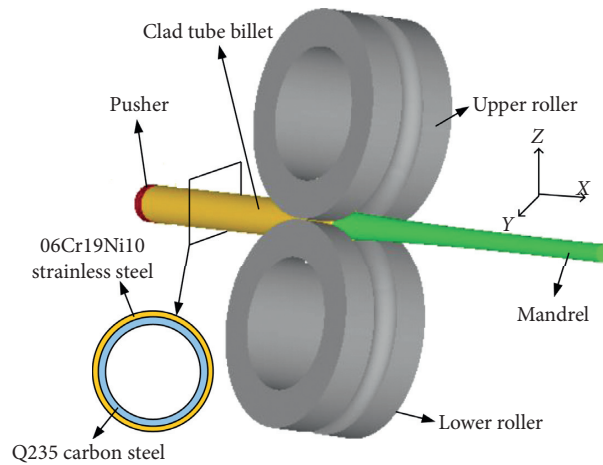


FIGURE 5: The finite element model of the pilger hot rolling bimetallic clad tube.

TABLE 1: Simulation parameters of the pilger hot rolling bimetallic clad tube.

Rolling speed (mm/sec)	Upper roller angular velocity (rad/sec)	Lower roller angular velocity (rad/sec)	Feed (mm)	Turning angle (°)	Friction coefficient between roller and outer tube	Coefficient of shear friction between inner and outer tubes	Temperature (°C)
1683.28	-10.0195	10.0195	10	57	0.1 [21]	0.5 [22]	1200

[10], as shown in Figure 1, the film formed by oxides, oil stains, and other impurities on the contact surface of the clad metal will be torn, and the fresh metal atoms on both sides will flow out and come into contact with one another. When the high dislocation density region is close to the ferrite/carbide interface, the carbon atoms will be attracted from the carbide until the dislocation is saturated [11–13]. This causes

carbon atoms to spread from the higher carbon potential carbon steel to the lower carbon potential stainless steel and to achieve metallurgy bonding.

At the beginning of the thermal deformation, the dislocation density increases with the increase of the metal strain. It is the joint result of work hardening and dynamic recovery softening. Figure 7 shows the true stress-strain

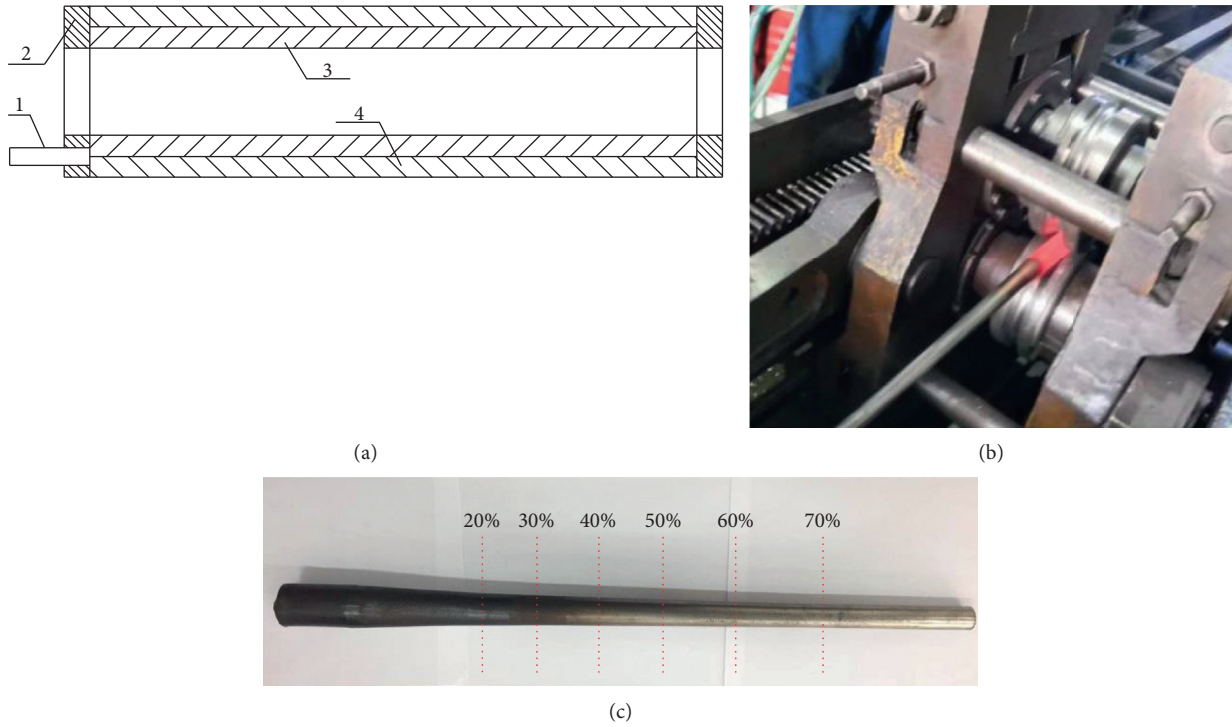


FIGURE 6: Experimental procedures of pilger hot rolling clad tube. (a) Blank forming. (b) Hot rolling process. (c) Sampling positions. 1, pumping tube; 2, seal weld; 3, carbon steel; 4, stainless steel.

TABLE 2: The chemical composition of carbon steel and stainless steel (wt%).

Elements	Fe	Cr	Ni	C	Mn	Si	P	S
06Cr ₁₉ Ni ₁₀	72.06	18.2	8.04	0.03	1.04	0.61	0.011	0.015
Q ₂₃₅	98.91	—	—	0.2	0.5	0.3	0.045	0.05

TABLE 3: The parameters of the clad tube billet.

Tube	Material	Outer diameter (mm)	Inner diameter (mm)	Length (mm)	Thickness ratio
Outer tube	06Cr ₁₉ Ni ₁₀ stainless steel	38	35	500	1 : 01
Inner tube	Q ₂₃₅ steel	35	32	500	

curve and hardening rate curve of 06Cr₁₉Ni₁₀ under different strain rates. It can be seen that work hardening exists when the initial strain is small. Figure 7(b) shows the work-hardening rate curve of the 06Cr₁₉Ni₁₀ stainless steel [23]. The degree of the work hardening increases with the increase of strain, but the work-hardening rate decreases as a whole because the metal becomes soft with the increase of stress on the metal and the dynamic recovery. Meanwhile, the growth of dislocation density in stainless steel also decreases because the rate of the work hardening decreases gradually.

As shown in Figure 4, the circumferential stress is not uniform in the process of pilger rolling clad tube, which leads to the uneven distribution of circumferential strain. Six cross sections are cut at different reduction rates along the X

TABLE 4: The parameters of the LG30 pilger rolling mill.

Parameter	Value
Crank radius (mm)	260
Length of connecting rod (mm)	1650
Eccentric distance (mm)	220
Main motor rated speed (r/min)	1000
Length of the mandrel (mm)	640
Length of deformation zone (mm)	384.67
Length of finishing zone (mm)	150
Feed (mm)	10
Turning angle (°)	57
Temperature (°C)	1200

direction of the rolled piece for the equivalent strain analysis, and the strain cloud diagram is shown in Figure 8. Since position *a* does not begin to deform, there is no thickness change and there is no strain. From position *b* to position *e*, the circumferential stress is not uniform in the process of plastic deformation. In the position *f*, the strain tends to be uniform. This is due to the fact that $B(x) = 0$ and the stress state of the clad tube is uniform three-dimensional compressive stress. Thus, it can be seen from the true stress-strain curve of stainless steel at 1200°C in Figure 7 and equation (1) that the dislocation density changes when carburizing occurs on the stainless steel layer in the pilger hot rolling clad process, which makes the thickness of the carburized layer change correspondingly.

The samples are cut and prepared for SEM from the clad tube with 30%, 50%, and 70% reduction rates at the corresponding positions in areas I, II, and III, as shown in Figure 4.

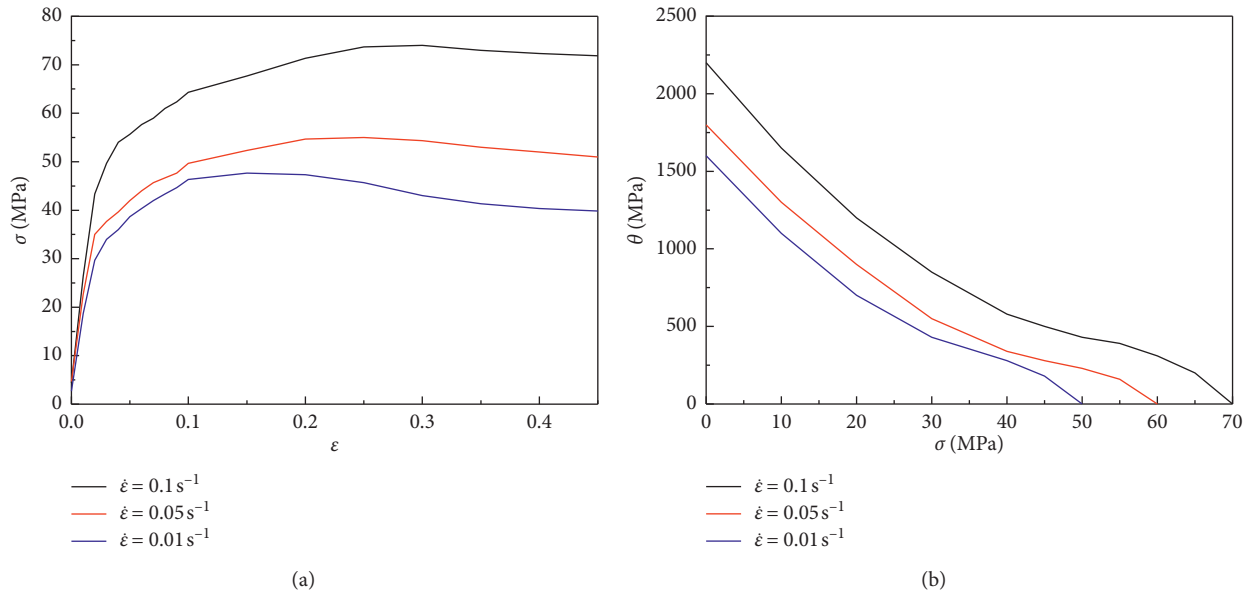


FIGURE 7: The true stress-strain and work-hardening rate curves of 06Cr₁₉Ni₁₀ stainless steel at different strain rates. (a) The true stress-strain curve. (b) The work-hardening rate curves.

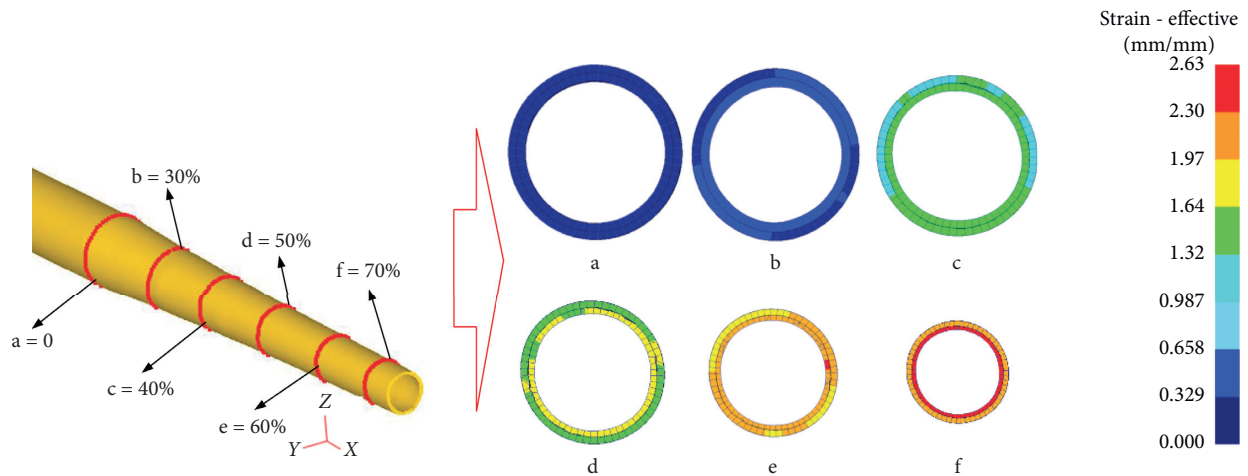


FIGURE 8: The equivalent strain nephogram of the outer and inner tubes at different reduction rates.

Figure 9 shows the SEM microstructure morphology at three points on the cross section of the rolled piece at 30% reduction rate. There are a lot of large particle contaminants in the bonding layer with discontinuous distribution. The carburized layers have been clearly formed in the three areas; however, the average thickness is different. Some areas have been fused and metallurgical bonding has been achieved.

Figure 10 shows the SEM microstructure morphology at three points on the cross section of the rolled piece at 50% reduction rate. The average thickness of the carburized layers is different at three points because different circumferential strains lead to the different dislocation densities on the side of stainless steel. A higher dislocation density results in a larger diffusion gradient on the side of the carbon steel, which makes the thickness of the carburized layers increase accordingly.

Figure 11 shows the SEM microstructure morphology at three points near the finishing zone at 70% reduction rate. The average thickness difference of the carburized layer has been approximately equal. It can be seen from Figure 8 that the circumferential strains of stainless steel have tended to be equal in the finishing zone; therefore, the dislocation densities near the bonding layer tend to be uniform, and the thickness of the carburized layer also tends to be the same.

From Figures 9–11, we can see the variation of carburized layer thickness shown in Figure 12(a); when the reduction rate of the clad tube is between 0 and 30%, the contaminants at the interface are gradually thinned and crushed with the increase of reduction rate, so that the metal atoms on both sides can meet. According to equation (1) and Figure 7, when stainless steel is on the early deformation stage, a large number of dislocations are generated due to

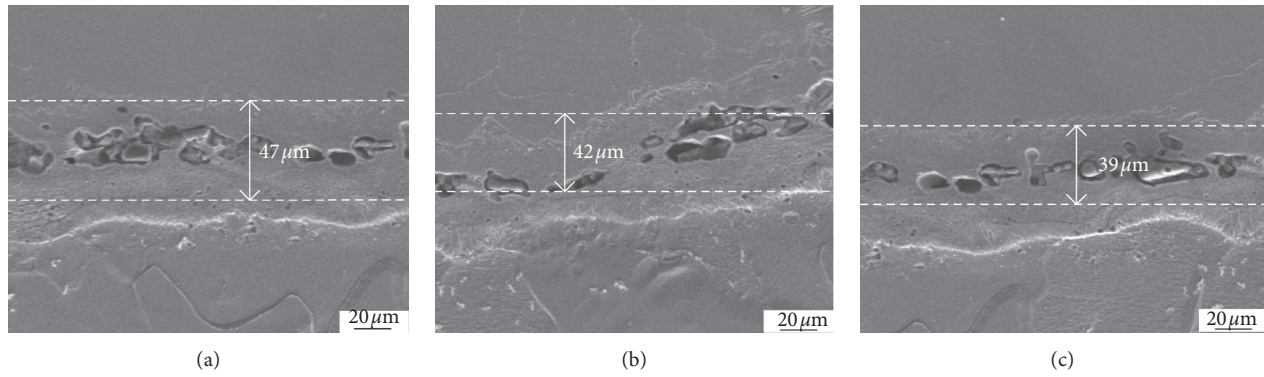


FIGURE 9: SEM morphology of the bonding layer with 30% reduction rate (500x). (a) Area I. (b) Area II. (c) Area III.

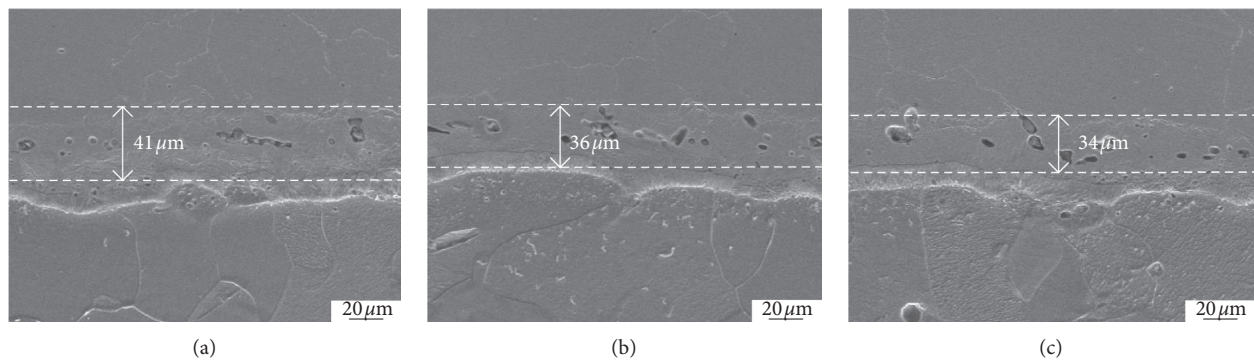


FIGURE 10: SEM morphology of the bonding layer with 50% reduction rate (500x). (a) Area I. (b) Area II. (c) Area III.

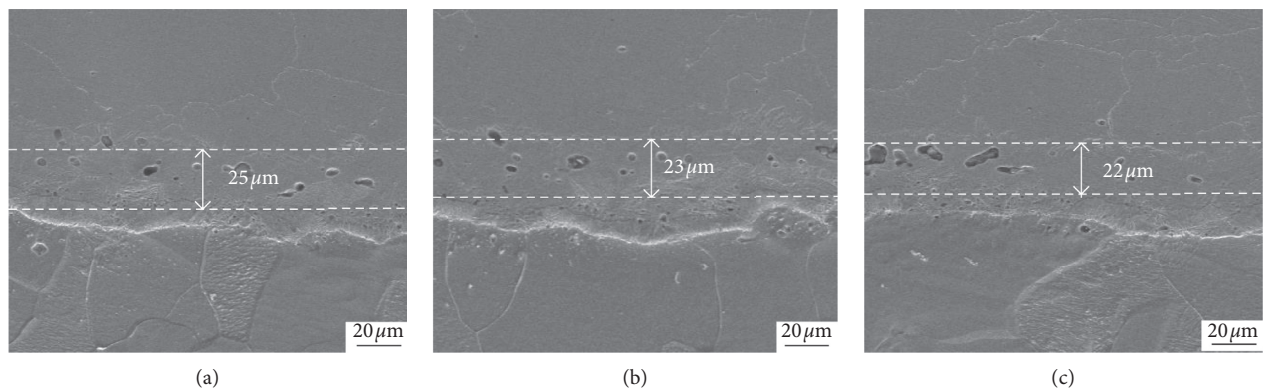


FIGURE 11: SEM morphology of the bonding layer with 70% reduction rate (500x). (a) Area I. (b) Area II. (c) Area III.

plastic deformation. At the same time, the carbon atoms in carbon steel begin to diffuse into the grain boundaries of the austenitic stainless steel and the carburized layer begins to appear. When the reduction rate increases from 30% to 70%, the thickness of carburized layer decreases along the axial direction. As shown in Figure 12(b), the thickness of the circumferential carburized layer is not uniform at different reduction rates. It is caused by the uneven circumferential stress of the pass at the pilger deformation section, which can be seen from equation (1) and Figure 8. The carburized layer in area I is thicker than that in area II and area III because area I always has one-dimensional axial tensile stress and

two-dimensional circumferential compressive stress state, as shown in Figure 4. The tensile stress makes the metal grains stretch along the axial direction, so that more fresh metal can be exposed on both sides, and the contaminants can be refined continuously. At the same time, a lot of dislocations are generated in the circumferential direction of stainless steel under the two-dimensional circumferential compressive stress, which makes the carbon atoms on the side of carbon steel diffuse. The effect is stronger than that of area II under the three-dimensional stress state and area III under the one-dimensional stress state, which ultimately leads to a higher thickness of carburized layer in area I than that in

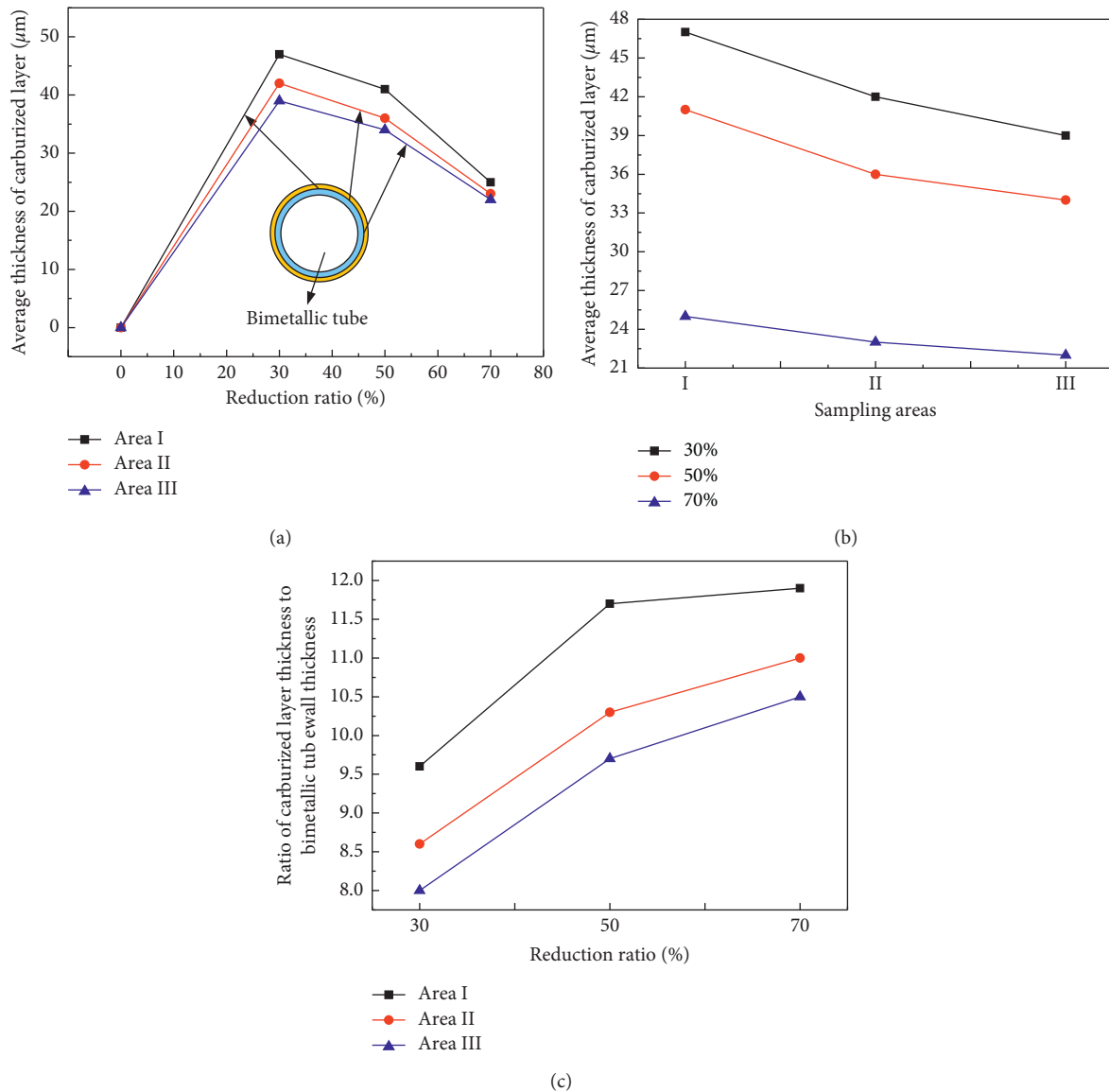


FIGURE 12: The variation of carburized layer thickness. (a) Different reduction rates. (b) Different sampling areas. (c) Ratio of carburized layer thickness to bimetallic tube wall thickness.

areas II and III. When the reduction rate reaches 70% near the finishing zone, the circumferential strain tends to be uniform and the thickness difference of the circumferential carburized layer is smaller, which can be seen from Figures 8 and 12(b). Figure 12(c) shows the ratio of the thickness of the carburized layer to the wall thickness of the clad tube under different reduction rates in three sampling areas. With the increase of reduction rate, the ratio is on the rise. It is indicated that, under the condition of large plastic deformation in the process of hot rolling, the metallurgical bonding degree is gradually increasing with the increase of reduction rate. In the later stage of deformation, as can be seen from Figure 7(b), with the increase of deformation, the work-hardening rate of stainless steel decreases continuously and enters the state of dynamic recrystallization, which gradually weakens the increasing speed of dislocation density, the carburizing ability, and the metallurgical bonding effect as well.

5.2. Diffusion Behavior of Carbon Atoms and Analysis of Precipitates. Figure 13 shows the SEM image of the bonding layer at 70% reduction rate. The EDS analysis was carried out on point *b* on the side of the stainless steel in Figure 13(a). As shown in Figure 13(b), the main components are carbon atoms and the content reaches 77.29%, besides other elements, such as Si, Mn, and O. It is indicated that a large number of carbon atoms have diffused into the side of the stainless steel. Si and Mn are the elements diffused from the carbon steel with C atom. O element is produced by oxidizing O_2 and Si, Mn, Fe, Cr, and S under low-vacuum condition. In Figure 13(a), it can be clearly seen that the carbide at the bonding surface has a certain directivity, and Xiao has found that the microstructure here is plate martensite [24]. Its cellular substructure, lower carbon content, and a lot of dislocation are caused by the large plastic deformation. A

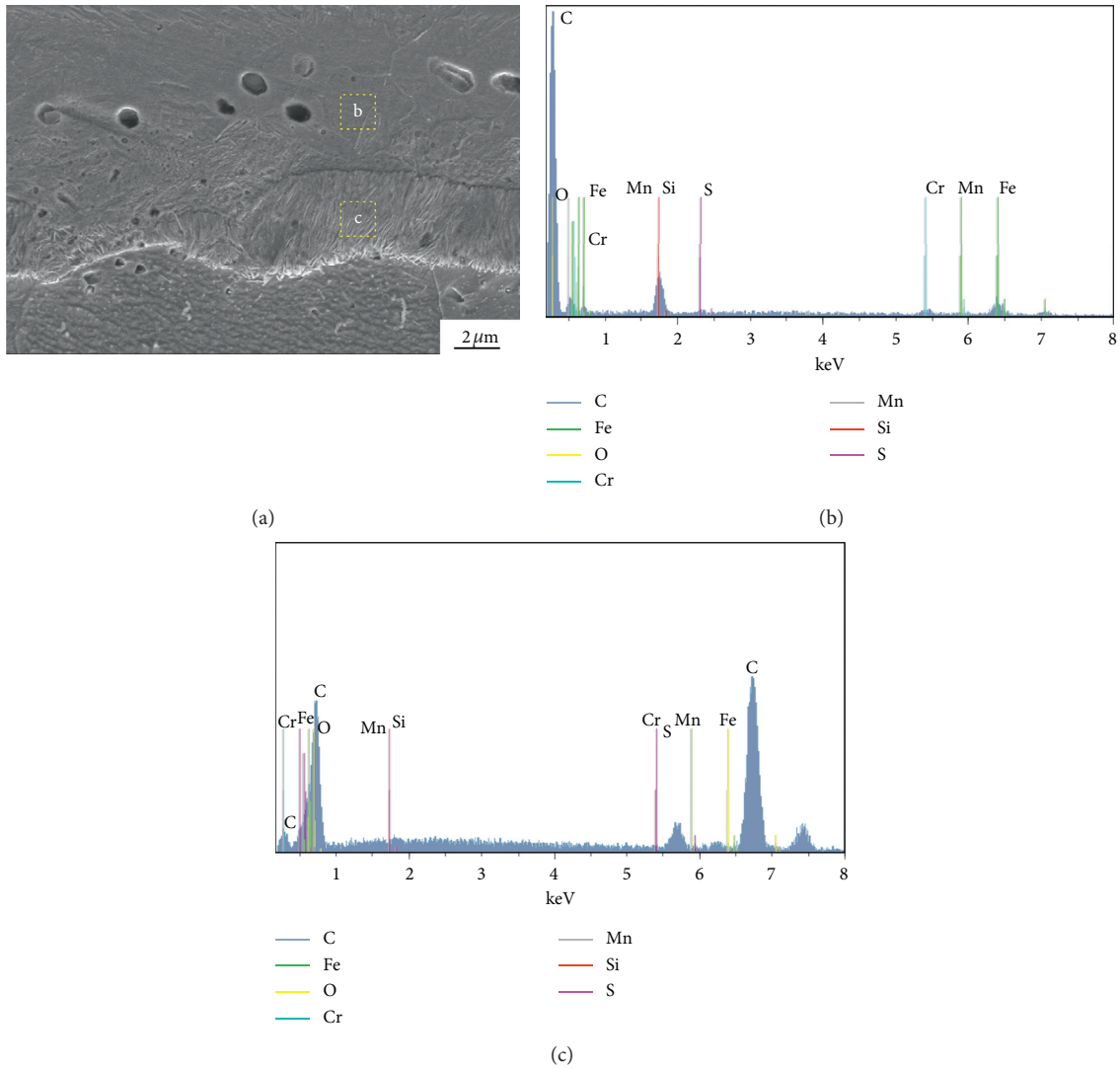


FIGURE 13: The SEM morphology of bonding layer at 70% reduction rate. (a) 2000x. (b) EDS at point b. (c) EDS at point c.

second EDS analysis was performed at point *c* near the bonding layer as shown in Figure 13(a) *c*. It is found in Figure 13(c) that the content of carbon is 7.01% at point *c*, and a diffusion zone of C atom is formed. At the same time, a large number of Cr atoms are found with the content of 5.84%. Liu has found that a new phase is formed at the bonding layer, and the main composition is Cr carbide [14].

Figure 14 shows the SEM microstructure morphology of the bonding layer at 60% reduction rate. Zone A is 06Cr₁₉Ni₁₀ stainless steel austenitic area, Zone B is the bonding layer, and Zone C is Q235 carbon steel. The number of pearlites within 50 microns on the side of carbon steel in the bonding layer decreases significantly, and there are no large pearlite structures; and the tiny pearlites are also discontinuously distributed along the bonding surface, which indicates that the decarburization occurs in the bonding layer. The line scan of Figure 14(a) shows that the number of Cr atoms, the main components of the stainless steel, have a distinct gradient variation from the stainless

steel to the carbon steel, which indicates that Cr atoms have also diffused, as shown in Figure 14(b).

The microstructure of Q235 steel is mainly the austenite structure at 1200°C. When the temperature drops to 550°C, the ferrite and the pearlite will be precipitated at the same time in the austenite. Meanwhile, the Q235 steel undergoes a phase transition and also generates ferrite and pearlite at the temperature of 1200°C under the rolling condition of large deformation. According to Clapeyron equation (2) [25], it is known that the steel has a phase transition under the internal stress. There are a lot of perlite particles distributing uniformly with large size (50 μm) and small size (2 μm), as shown in the Zone C of Figure 14(a). According to Clapeyron equation (2), this is due to the refinement of the pearlite grains under a large rolling force:

$$\frac{dF}{d \ln T} = \frac{\Delta H^{1 \rightarrow 2}}{\Delta V^{1 \rightarrow 2}}, \quad (2)$$

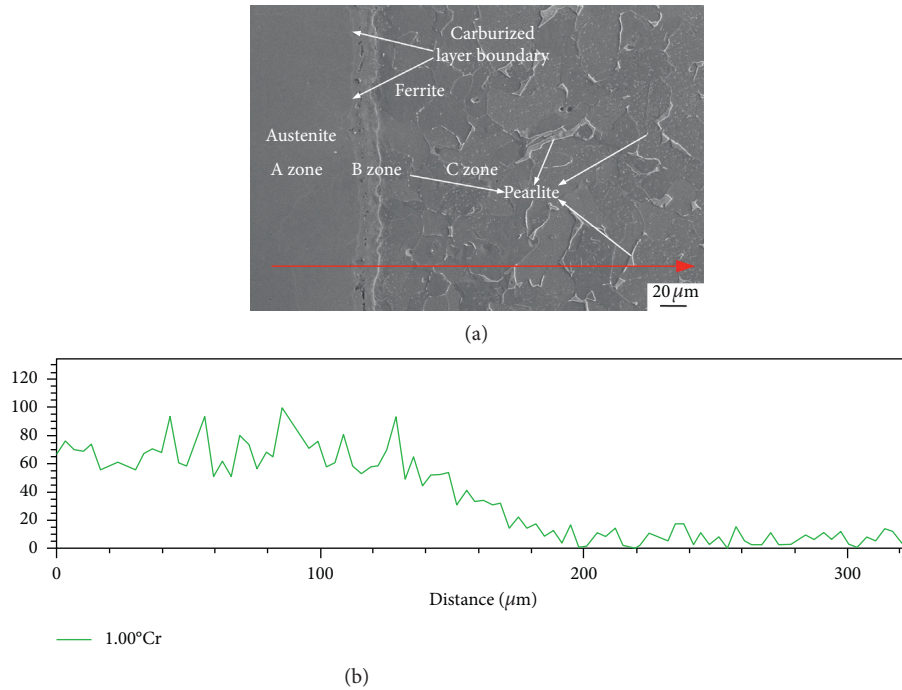


FIGURE 14: The SEM morphology of bonding layer at 60% reduction rate. (a) 200x. (b) Line scan.

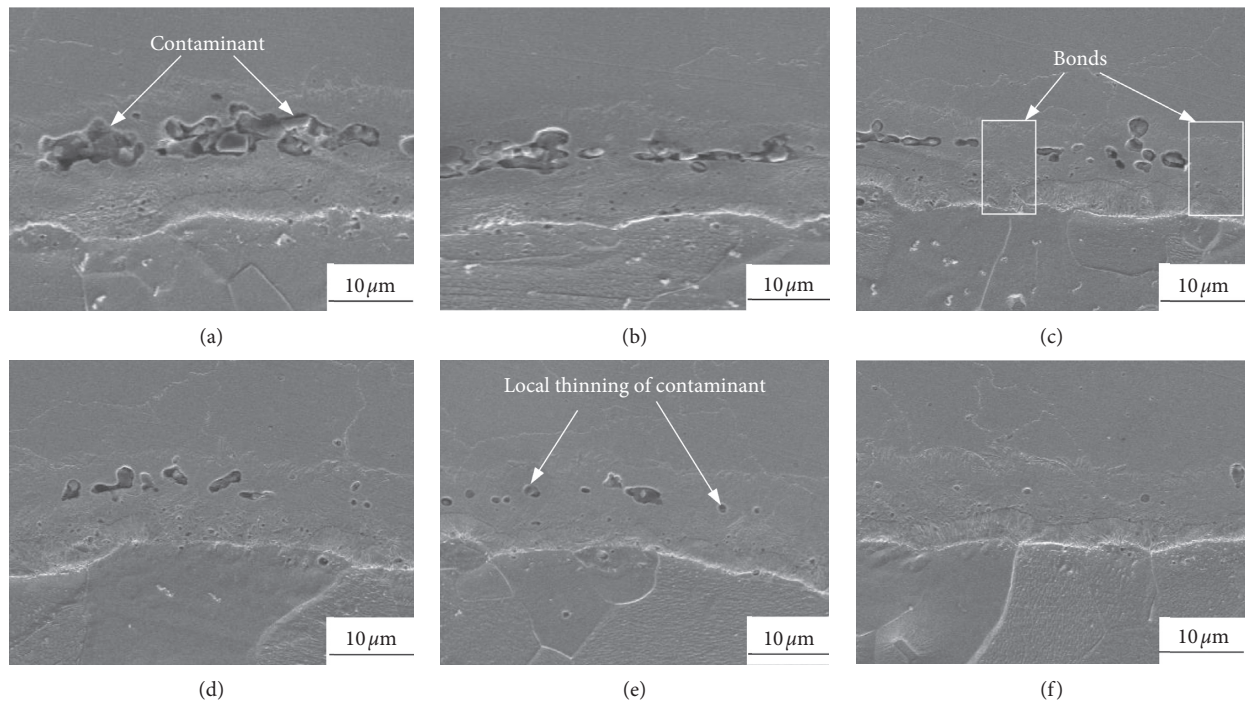


FIGURE 15: The SEM morphology of bonding layer at different reduction rates (1000x). (a) 20% reduction rate. (b) 30% reduction rate. (c) 40% reduction rate. (d) 50% reduction rate. (e) 60% reduction rate. (f) 70% reduction rate.

where $\Delta H^{1 \rightarrow 2}$ is the phase transition heat enthalpy; $\Delta V^{1 \rightarrow 2}$ is the volume change after a phase transition; F is the pressure; and T is the temperature.

The transformation of the austenite to the pearlite in carbon steel is caused by phase transition, and the pearlite is gradually crushed and refined by the cumulative

deformation of the pilger rolling. The fine pearlite particles near the bonding surface make the carbon atoms more uniformly distributed along the bonding surface. When the dislocation and the diffusion occur at the interface, the homogeneous carbon atoms are more likely to diffuse directly, and the carbon atoms in the tiny pearlite are directly

diffused to the opposite dislocation area, thus forming a large ferrite area. The large pearlite particles are further refined by the internal stress under the large deformation. Therefore, a discontinuous distribution of the pearlite particles appears, as shown in Figure 14(a).

Figure 15 shows the microstructure of the bonding layer at the position shown in Figure 6(a) at 6 different reduction rates. It can be seen from Figures 15(a) and 15(b) that when the reduction rate of the clad tube is 20%~30%, a lot of black flocculent materials appear near the bonding layer. According to the thin film theory [10], the materials are the contaminants on the bonding layer, mainly composed of metal oxides and interfacial impurities. With the increase of the reduction rate, it can be seen from Figures 15(c) and 15(d) that the size of the contaminants decreases significantly, while the spacing increases constantly. When the reduction rate reaches 60%~70%, the contaminants are further refined, as shown in Figures 15(e) and 15(f), because the local pressure leads to the expansion of the metal surface, which causes the rupture of contaminants on the surface of the two metals and the leakage of the fresh metal. The fresh metal fusion on two sides makes the initial large contaminants separated. With the gradual increase of metal plastic deformation, more and more fresh metal is exposed on both sides, and the contaminants are further refined. Some studies have shown that the finer contaminants are more beneficial to the bimetallic metallurgical bonding [26].

6. Conclusions

- (1) In the metallurgical bonding process of pilger hot rolling carbon steel and stainless steel tube, the diffusion of carbon atom is related to the degree of plastic deformation of stainless steel. In the early stage, the deformation of stainless steel is small, dislocation density increases sharply, the carburized layer appears and becomes thicker, and its maximum thickness is $47\ \mu\text{m}$ at 30% reduction rate. With the increase of deformation, the thickness of carburized layer decreases and the minimum thickness is $22\ \mu\text{m}$ at 70% reduction rate. The thickness difference of circumferential carburized layer near the finishing zone of clad tube is smaller than that in the deformation zone.
- (2) With the increase of deformation, the work-hardening rate of stainless steel decreases continuously and enters the state of dynamic recrystallization, which gradually weakens the increasing speed of dislocation density, the carburizing ability, and the metallurgical bonding effect as well.
- (3) The contaminants in the bonding layer are refined gradually with the increase of the reduction rate, and the size of contaminant particles is less than $2\ \mu\text{m}$ at 70% reduction rate. The new structures, martensitic structures, are formed in the bonding layer by the diffusion of carbon atoms. The chromium carbides are formed by combining the diffused carbon atoms with the diffused Cr atoms.
- (4) The carbon steel and the stainless steel tube can be completely rolled by the pilger hot rolling so that the excellent metallurgical bonding is formed.

Data Availability

All data used to support the findings of this study are included within the article. More detailed data can be made available from the authors upon request.

Conflicts of Interest

The authors declare that there are no conflicts of interest regarding the publication of this paper.

Acknowledgments

This work was supported by the National Natural Science Foundation of China (no. U1710113) and Shanxi Provincial Key Research and Development Project (no. 2018YFB1307902).

References

- [1] J. L. Alcaraz, J. Gil-Sevillano, and J. M. Martínez-Esnaola, "A fracture condition based on the upper bound method for the extrusion of bimetallic tubes," *Journal of Materials Processing Technology*, vol. 61, no. 3, pp. 265–274, 1996.
- [2] H. D. Wright, T. O. S. Oduyemi, and H. R. Evans, "The experimental behaviour of double skin composite elements," *Journal of Constructional Steel Research*, vol. 19, no. 2, pp. 97–110, 1991.
- [3] C. Wang, Z. Y. Bi, W. P. Zhang, Y. B. Yang, and C. C. Han, "Research status on double-metal composite pipe at home and abroad," *Welded Pipe and Tube*, vol. 38, no. 12, pp. 7–12, 2015.
- [4] Y. F. Wang, S. D. Zhao, and C. Y. Zhang, "Research status and development of forming technology for bi-metal-lined pipe," *China Metal Forming Equipment & Manufacturing Technology*, vol. 24, no. 3, pp. 84–89, 2015.
- [5] G. P. Gong, "Extrusion process for manufacturing bimetal clad pipes," *Steel Pipe*, vol. 43, no. 2, pp. 36–40, 2014.
- [6] X. F. Fan and T. X. Xu, "Explosive recombination of Ta-10W liner and steel pipe," *Rare Metal Materials and Engineering*, vol. 42, no. 2, pp. 55–58, 1995.
- [7] W. Y. Zhang, "Research and application of bimetal composite pipe," *Dynamic State at Home and Abroad*, vol. 70, no. 3, pp. 71–72, 2016.
- [8] H. Nie, W. Liang, H. Chen, X. Hao, C. Chi, and X. Li, "Vacuum hot pressed AZ31/UCF/AZ31 composite sheets: microstructure and mechanical properties," *Vacuum*, vol. 144, no. 10, pp. 247–255, 2017.
- [9] Y. Ding, R. Cao, and Y. J. Yan, "Effects of heat treatment on fracture mechanism of martensite/austenite MLS composite plates by hot roll bonding," *Materials Science and Engineering: A*, vol. 773, no. 31, Article ID 138727, 2017.
- [10] Y. S. Wang, W. Y. Li, X. W. Yang, and Y. Fu, "Research status on interface bonding mechanisms and strength of cold pressure welding," *Journal of Materials Engineering*, vol. 44, no. 4, pp. 119–130, 2016.
- [11] J.-H. Kang and P. E. J. Rivera-Díaz-del-Castillo, "Carbide dissolution in bearing steels," *Computational Materials Science*, vol. 67, pp. 364–372, 2013.

- [12] M. Suehiro and Y. Hashimoto, "Carbon distribution near interface between base and cladding steels in austenite stainless clad steel sheet," *Tetsu-to-Hagane*, vol. 75, no. 9, pp. 1501–1507, 1989.
- [13] T. Kushida and T. Kudo, "Hydrogen disbonding of stainless clad steels by cathodic current," *Tetsu-to-Hagane*, vol. 75, no. 9, pp. 1508–1514, 1989.
- [14] B. X. Liu, S. Wang, W. Fang, F. X. Yin, and C. X. Chen, "Meso and microscale clad interface characteristics of hot-rolled stainless steel clad plate," *Materials Characterization*, vol. 148, pp. 17–25, 2019.
- [15] X. L. Dai, B. X. Liu, J. L. Ma, J. Y. Wei, and F. X. Yin, "Microstructure and mechanical properties of stainless steel clad plate fabricated by vacuum hot rolling," *Iron & Steel*, vol. 52, no. 2, pp. 65–70, 2017.
- [16] X. W. Chen, J. Y. Wang, X. Q. Yang, T. Huang, and K. X. Song, "Hot deformation behavior and dislocation density evolution regularity of Cr8 alloy," *Journal of Jilin University*, vol. 50, no. 1, pp. 91–99, 2020.
- [17] Z. C. Yu and Z. M. Ren, "Application and development of two high periodic cold rolling mill in copper alloy pipe production," *Chinese High-Tech Enterprises*, vol. 27, pp. 41–43, 2013.
- [18] Z. B. Chu, D. Zhang, and D. Wei, "Study on microstructure evolution of pilger cold rolled seamless steel tube," *Advanced Engineering Sciences*, vol. 49, no. 6, pp. 63–170, 2017.
- [19] Y. D. Yin, M. J. Wang, D. Z. Li, and H. J. Chen, "Analysis on transverse wall thickness accuracy of pilger cold rolled tube," *Hot Working Technology*, vol. 45, no. 5, pp. 163–166, 2016.
- [20] D. Wei, Z. B. Chu, and Q. X. Huang, "Finite element simulation and analysis of Pilger cold-rolling of stainless steel tube based on DEFORM-3D," *Journal of Plasticity Engineering*, vol. 23, no. 5, pp. 89–95, 2016.
- [21] P. Montmitonnet, R. Logé, M. Hamery, Y. Chastel, J.-L. Doudoux, and J.-L. Aubin, "3D elastic-plastic finite element simulation of cold pilgering of zircaloy tubes," *Journal of Materials Processing Technology*, vol. 126, pp. 814–820, 2002.
- [22] H. R. Jin, M. F. Han, and C. X. Duan, "Effect of reduction rates on interfacial microstructure morphologies of 316L/EH40 clad plate," *Iron & Steel*, vol. 54, no. 12, pp. 62–69, 2019.
- [23] Q. L. Hao, *Research on Seamless Techniques and Equipment Development for Medium or Small Caliber HFW Tubes*, University of Science and Technology, Beijing, China, 2018.
- [24] X.-F. Xiao, S.-P. Ye, W.-X. Yin, and Q. Xue, "HCWCI/carbon steel bimetal liner by liquid-liquid compound lost foam casting," *Journal of Iron and Steel Research International*, vol. 19, no. 10, pp. 13–19, 2012.
- [25] H. B. Li, Q. X. Huang, and C. L. Zhou, "Microstructure evolution of carbon steel at interface of carbon steel/stainless steel clad plate by hot rolling," *Transactions of Materials and Heat Treatment*, vol. 35, no. 4, pp. 57–61, 2014.
- [26] X. K. Peng, R. Wuhner, G. Heness, and W. Y. Yeung, "Rolling strain effects on the interlaminar properties of roll bonded copper/aluminum metal laminates," *Journal of Materials Science*, vol. 35, no. 17, pp. 4357–4363, 2000.